ELSEVIER

Volume 211 March 2014 ISSN 0022-4596

JOURNAL OF SOLID STATE CHEMISTRY

IN THIS ISSUE:

Synthesis, structure, and magnetic properties of the novel sodium cobalt tellurate $Na_5Co_{15.5}Te_6O_{36}$

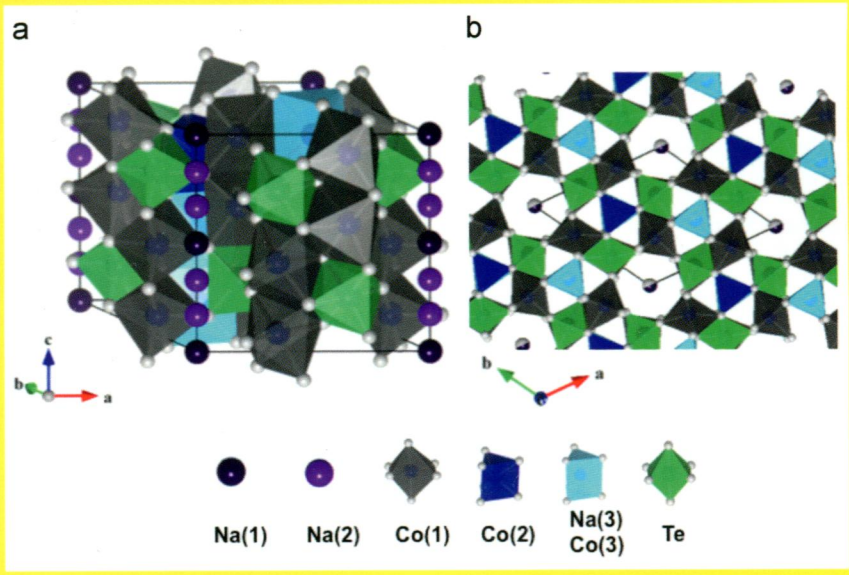

Yue Jin Shan, Yuta Yoshioka, Makoto Wakeshima, Keitaro Tezuka and Hideo Imoto

ELSEVIER

Volume 211, March 2014

JOURNAL OF SOLID STATE CHEMISTRY

www.elsevier.com/locate/jssc

CONTENTS

Abstracted/indexed in BioEngineering Abstracts, Chemical Abstracts, Coal Abstracts, Current Contents/Physics, Chemical, & Earth Sciences, Engineering Index, Research Alert, SCISEARCH, Science Abstracts, and Science Citation Index. Also covered in the abstract and citation database SCOPUS®. Full text available on ScienceDirect®.

Regular Articles

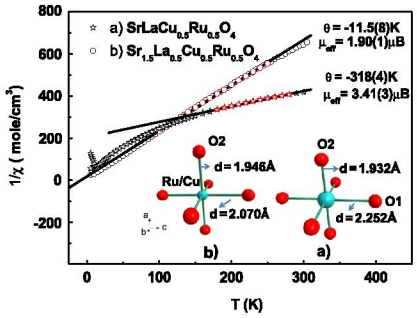

$SrLaCu_{0.5}Ru_{0.5}O_4$ with K_2NiF_4-type structure show a larger static Jahn–Teller distortion than $Sr_{1.5}La_{0.5}Cu_{0.5}Ru_{0.5}O_4$, which may be related to stronger antiferromagnetic superexchange interactions.

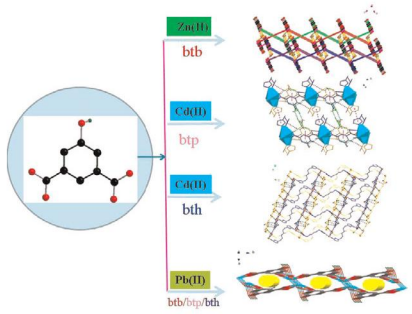

Among four 2D CPs reported, **1** is an unusual 2D→3D polythreaded framework. **4** exhibits 2D double-layered binodal (4, 4)-net containing nanochannels. Reversible dehydration–rehydration is observed in **1**, **2** and **4**.

Regular Articles—Continued

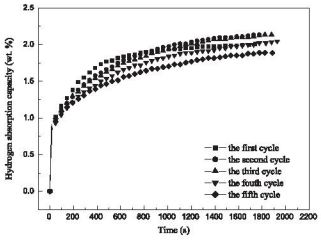

Hydrogen absorption curves of $LiBH_4$ doped with MoS_2 for five cycles at 400 °C.

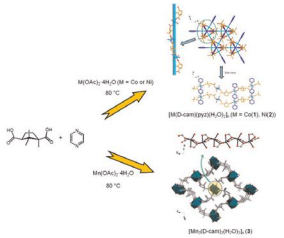

The preparations and properties of three new homochiral three-dimensional (3D) coordination polymers, $[M(D\text{-cam})(pyz)(H_2O)_2]_n$ (M=Co (**1**) and Ni (**2**); D-H_2cam=(+) D-camphoric acid; pyz=pyrazine) and $[Mn_2(D\text{-cam})_2(H_2O)_2]$ (**3**), under solvothermal conditions is described. Single-crystal X-ray diffraction analyses revealed that all of compounds are homochiral 3D structure. **1** and **2** are isostructural and crystallize in the trigonal space group $P3_221$, while **3** crystallizes in monoclinic space group $P2_1$. The structure of **1** and **2** consists of metal-D-cam helical chains which are pillared with pyrazine ligands into a 3D framework structure and **3** features a 3D homochiral framework involving one-dimensional manganese-carboxylate chains that are aligned parallel to the b axis. Magnetic susceptibility data of all compounds were collected. The findings indicate that μ_2-pyrazine dominate weak antiferromagnetic coupling within **1** and **2**, while **3** exhibits antiferromagnetic behavior through the carboxylate groups of D-cam ligand.

Continued

Cooperative upconversion luminescence in Tb^{3+}:Yb^{3+} co-doped Y_2SiO_5 powders prepared by combustion synthesis

Nikifor Rakov, Simone A. Vieira, Renato B. Guimarães and Glauco S. Maciel

page 32

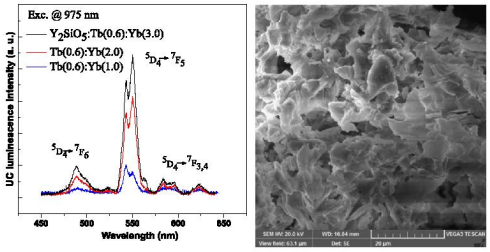

Left: Cooperative upconversion luminescence spectra of three powder samples prepared by combustion synthesis. Right: The SEM image of the powder showing that it consists of agglomerated flake-like shaped particles of various sizes. Full scale bar is 20 μm.

Preparation and structural, optical, magnetic, and electrical characterization of Mn^{2+}/Co^{2+}/Cu^{2+} doped hematite nanocrystals

S.I. Srikrishna Ramya and C.K. Mahadevan

page 37

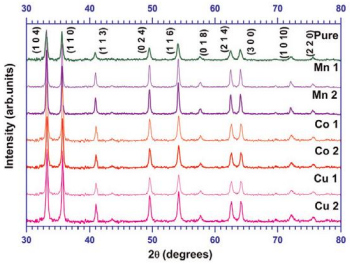

The indexed X-ray diffraction (XRD) patterns of all the seven nanocrystals indicate the rhombohedral structure of hematite (JCPDS card No.13-0534). No impurity phase like oxides of Mn or Co or Cu was detected above equipment limit. The average crystallite (grain) sizes estimated using the Scherrer's formula.

Preparation, characterization and catalytic properties of MCM-48 supported tungstophosphoric acid mesoporous materials for green synthesis of benzoic acid

Hai-Yan Wu, Xiao-Li Zhang, Xi Chen, Ya Chen and Xiu-Cheng Zheng

page 51

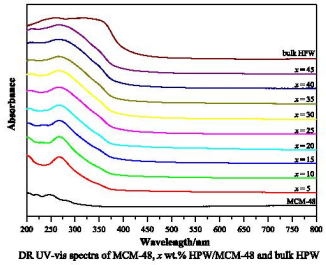

DR UV-vis spectra of MCM-48, *x* wt.% HPW/MCM-48 and bulk HPW

Investigation of phase evolution of $CaCu_3Ti_4O_{12}$ (CCTO) by *in situ* synchrotron high-temperature powder diffraction

Xin Ouyang, Saifang Huang, Weijun Zhang, Peng Cao, Zhaohui Huang and Wei Gao

page 58

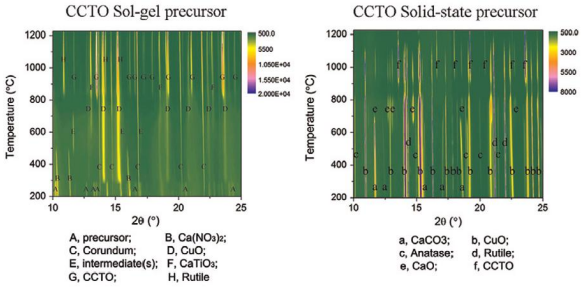

The *in situ* synchrotron HT-XRD patterns of CCTO sol–gel and solid-state precursor.

Synthesis, structure, and magnetic properties of the novel sodium cobalt tellurate $Na_5Co_{15.5}Te_6O_{36}$

Yue Jin Shan, Yuta Yoshioka, Makoto Wakeshima, Keitaro Tezuka and Hideo Imoto

page 63

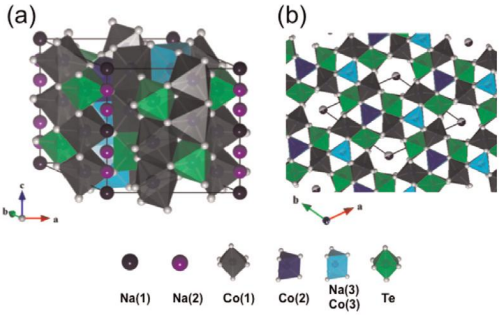

The unit cell (a) and perspective view along [001] (b) of novel single crystal oxide, $Na_5Co_{15.5}Te_6O_{36}$.

Preparation and thermal stability of the spindle α-Fe_2O_3@SiO_2 core–shell nanoparticles

Xin Zhang, Yongan Niu, Yang Li, Yao Li and Jiupeng Zhao

page 69

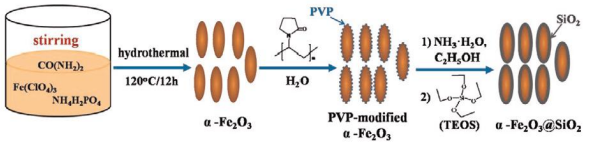

Schematic of preparation of the monodisperse spindle α-Fe_2O_3@SiO_2 nanoparticles (NPs).

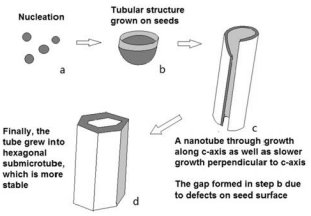

A convenient solvothermal approach was applied to synthesize In_2Te_3 nanotubes, which has not been reported in the literature for our knowledge. Surface area of this material is 137.85 $m^2\ g^{-1}$ from the BET testing, and such a high value makes it probably suitable for gas sensing and hydrogen storage, compared with the nanowires. The nanotube device also has a broad light detection range from 300 nm to 1100 nm, covering the UV–visible–NIR region. This good performance of In_2Te_3 nanotubes may enable significant advancements of new photodetection and photosensing applications.

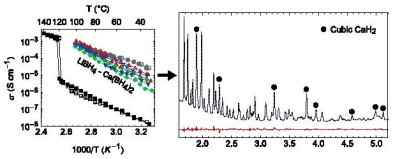

An Arrhenius plot of the ionic conductivity of the $LiBH_4$–$Ca(BH_4)_2$ composites (red, blue, green). The ionic conductivity of ball milled (gray) and non-milled (black) $LiBH_4$ is shown for comparison. The filled symbols are measured during heating runs and the empty symbols are measured during subsequent cooling runs. The conductivity of the composites is in all cases higher during cooling, most probably due to the formation of an electronically conducting layer containing defect-rich cubic CaH_2. Such layer formation could eventually lead to a short circuit in the cell and reveals a general issue of chemical stability that should be attended to in the development of solid electrolyte materials.

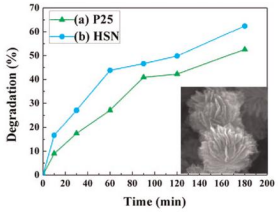

Novel TiO_2 with anatase micro-spheres and rutile nanobelts is synthesized. Enhanced photocatalysis is attributed to hierarchical structures (3D spheres), conductive channel (1D nanobelts) and large specific surface area (2D nanosheet).

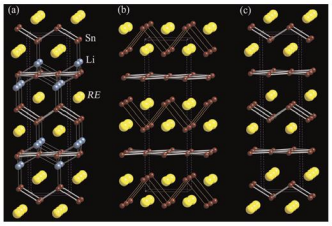

$RELi_xSn_2$ (RE=La–Nd, $0 \le x < 1$) crystallize in a defect variants of the $CeNiSi_2$ structure type (a). The Sn-disorder and the Li-deficiency correlate, and vary monotonically with the decreased size of the rare-earth atoms in the order RE=La–Nd. The $SmSn_2$ (b) and $GdSn_2$ (c) structures are devoid of any disorder.

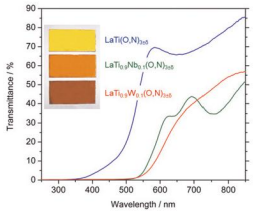

The synthesis of $LaTi_{1-x}M_x(O,N)_{3\pm\delta}$ (x=0; 0.1, M=Nb^{5+}, W^{6+}) thin films by microwave-induced plasma ammonolysis is described and changes of their optical and transport properties upon B-site substitution are discussed.

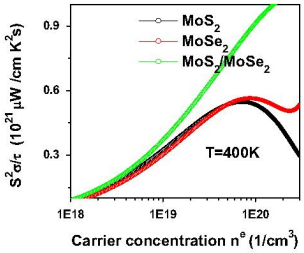

On the basis of density functional calculations we predict that the mixed-layer compounds 2H-MoS_2/2H-$MoSe_2$, in which two different layers 2H-MoS_2 and 2H-$MoSe_2$, have enhanced thermoelectric properties because of the increased density of states around the Fermi level and the decreased band gap size.

Continued

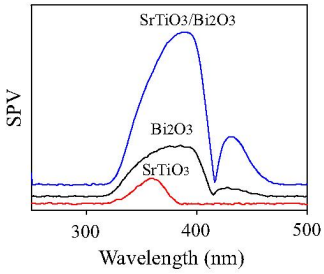

Enhanced separation efficiency for $SrTiO_3/Bi_2O_3$ is resulting from the energy difference between the conduction band edges.

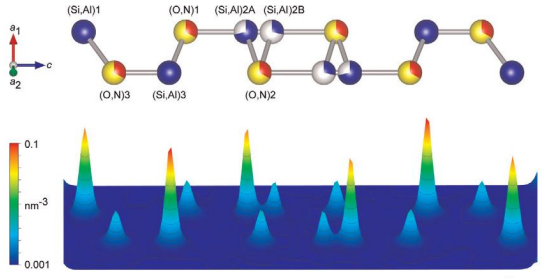

A bird's eye view of electron densities up to 75.3% (0.133 nm^{-3}) of the maximum on the plane parallel to (110) with the corresponding atomic arrangements of $SiAl_4O_2N_4$.

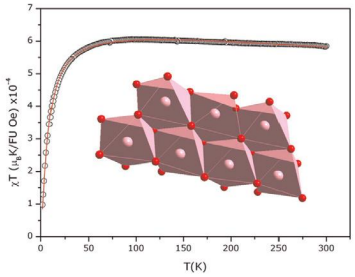

A manganese silicate prepared hydrothermally with formula $NaMn_2Si_3O_8(OH)$ possessing the structure of the mineral Serandite contains doubled chains of edge-sharing MnO_6 octahedra. The magnetic susceptibility was measured and shows an antiferromagnetic behavior.

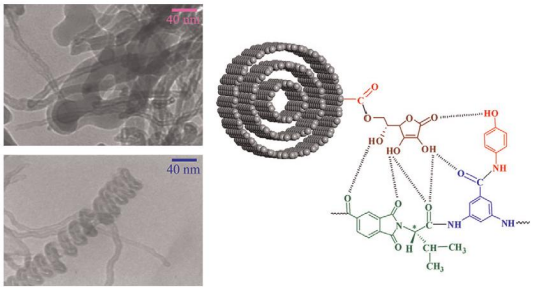

Presentation of possible interactions of hydrogen bonding between the MWCNT-AS and the PAI chains.

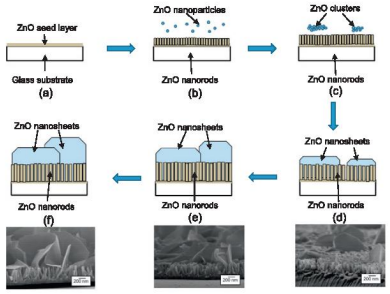

Schematic illustration of ZnO nanorod–nanosheet composite structure formation by hydrothermal at low-temperature of 80 °C against time.

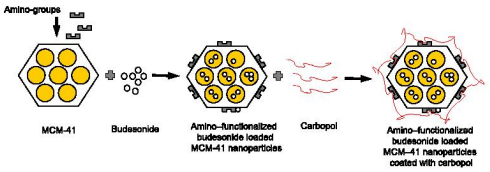

Silica mesoporous MCM-41 particles were amino-functionalized, loaded with budesonide and post-coated with bioadhesive polymer (carbopol) in order to achieve prolonged residence of anti-inflammatory drug in GIT.

Fundamental research on gas–solid reaction between CO_2 and Li_2CuO_2 linking application for solid CO_2 absorbent
Katsuyoshi Oh-ishi, Yusuke Matsukura, Takeshi Okumura, Yuuki Matsunaga and Ryota Kobayashi
page 162

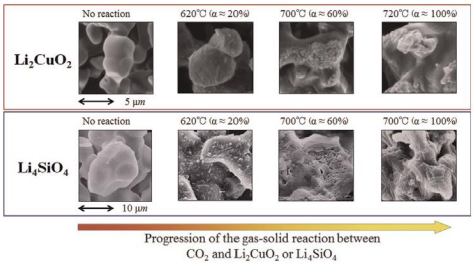

Surface changes of Li_2CuO_2 and Li_4SiO_4 particles by progression of the gas–solid reactions between CO_2 and these oxides.

Lithium-cation conductivity and crystal structure of lithium diphosphate
V.I. Voronin, E.A. Sherstobitova, V.A. Blatov and G.Sh. Shekhtman
page 170

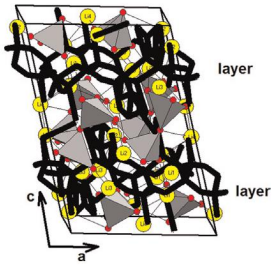

Crystal structure of $Li_4P_2O_7$ at 950 K. Red balls represent oxygen atoms; black lines show Li^+ ion migration channels in the layers perpendicular to [001] direction.

Controlled synthesis of T-shaped $BiVO_4$ and enhanced visible light responsive photocatalytic activity
Shuying Dong, Chongfei Yu, Yukun Li, Yihui Li, Jianhui Sun and Xiaofei Geng
page 176

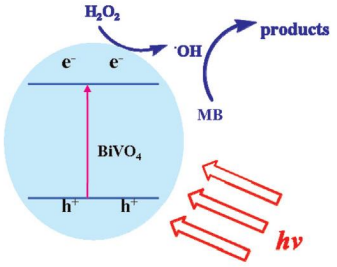

H_2O_2 molecules function as electron trapping reagent to react with e^- to enhance the photocatalytic degradation efficiency of MB in the $BiVO_4$/H_2O_2 system under visible light irradiation.

Synthesis, crystal structure and electronic properties of the new iron selenide $Ba_9Fe_4Se_{16}$
David Berthebaud, K.R.S. Preethi Meher, Denis Pelloquin and Antoine Maignan
page 184

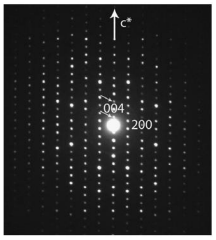

Experimental electron diffraction (ED) patterns of $Ba_9Fe_4Se_{16}$ recorded along a-[010].

Fast, selective adsorption of Cu^{2+} from aqueous mixed metal ions solution using 1,4,7-triazacyclononane modified SBA-15 silica adsorbent (SBA-TACN)
Pradip Kumar Tapaswi, Madhappan Santha Moorthy, Sung Soo Park and Chang-Sik Ha
page 191

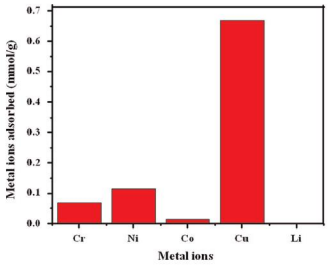

A new SBA-15 supported 1,4,7-triazacyclononane (TACN) modified mesoporous silica (SBA-TACN) adsorbent has been developed which shows excellent selectivity in Cu^{2+} adsorption from aqueous mixed metal ion solutions at pH 5. The copper ion adsorption capacity of the SBA-TACN can reach a maximum value of 0.67 mmol/g. The adsobent is stable enough to be used atleast for three cycles.

Synthesis and characterization of two polyoxometalates consisting of different Cu-ligand hydrogen phosphate units
Jinshuang Yan, Xiaofang Zhao, Jiao Huang, Kaining Gong, Zhangang Han and Xueliang Zhai
page 200

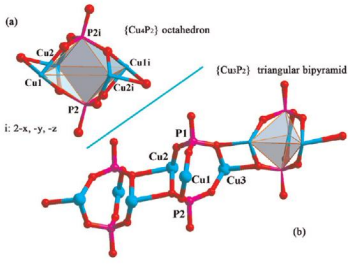

Two polyoxometalate-based supramolecular compounds consisting of different linkages based on Cu-ligand and HPO_4^{2-} groups have been synthesized and characterized. The photocatalytic activity are studied.

Continued

$Yb_{14-x}Tm_xMnSb_{11}$ ($0<x<0.5$): Structure and magnetic properties

John H. Roudebush, Jason Grebenkemper, Yufei Hu, Nasrin Kazem, M.N. Abdusalyamova and Susan M. Kauzlarich

page 206

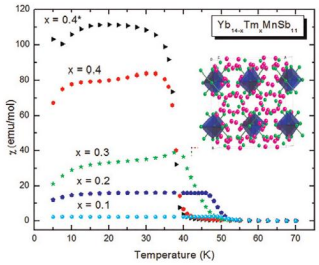

Magnetic susceptibility (χ) for $Yb_{14-x}Tm_xMnSb_{11}$ at H_a=0.01 T as a function of temperature along with a view of the structure.

Lithium vanadyl oxalatophosphite: Influence of the water content on the crystal structures and the dehydration scheme

S. Auguste, V. Alonzo, T. Bataille, L. Le Pollès, W. Cañón-Mancisidor, D. Venegas-Yazigi and E. Le Fur

page 212

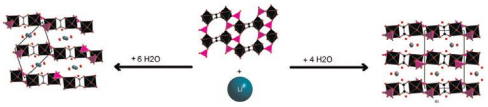

Two new lithium vanadyl oxalatophosphites layered compounds, $Li_2(VOHPO_3)_2C_2O_4$ $6H_2O$ (**1**) and Li_2 $(VOHPO_3)_2C_2O_4$ $4H_2O$ (**2**) have been hydrothermally synthesized. Lithium ions and water molecules are located between the anionic $[(VO)_2(HPO_3)_2C_2O_4]^{2-}$ layers. Thermal behaviors were carefully studied by thermogravimetric and thermal dependant X-ray diffraction. Various intermediate phases were evidenced and for both compounds the final product was $LiVOPO_4$.

Low-field magnetoresistance up to 400 K in double perovskite Sr_2FeMoO_6 synthesized by a citrate route

L. Harnagea, B. Jurca and P. Berthet

page 219

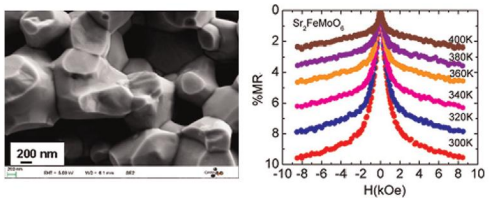

The microstructure (left panel) and corresponding low-field magnetoresistance of one of the Sr_2FeMoO_6 samples synthesized in the course of this work.

Electronic, structural and magnetic studies of niobium borides of group 8 transition metals, Nb_2MB_2 (M=Fe, Ru, Os) from first principles calculations

Rachid St. Touzani and Boniface P.T. Fokwa

page 227

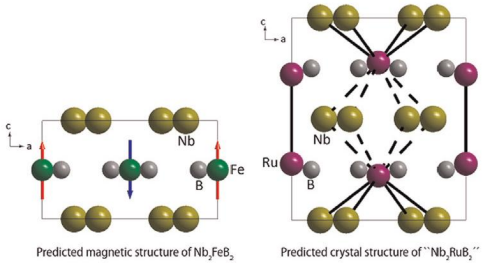

Nb_2FeB_2 (U_3Si_2 structure type, space group *P4/mbm*, no. 127) is predicted to order antiferromagnetically, due to the presence of iron chains which show ferromagnetic interactions in the chains and antiferromagnetic interactions between them. "Nb_2RuB_2" is predicted to crystallize with the recently discovered Nb_2OsB_2 twofold superstructure (space group *P4/mnc*, no. 128) of U_3Si_2 structure type. The building of ruthenium dumbbells instead of chains along [001] is found to be responsible for the stabilization of this superstructure.